Shape of the electron capture to the continuum cusps for H, H_2, and He targets in the velocity range 6.3—18.0 a.u.

S. D. Berry, G. A. Glass,* I. A. Sellin, K.-O. Groeneveld,† D. Hofmann,†
L. H. Andersen,‡ M. Breinig, S. B. Elston, P. Engar, and M. M. Schauer§
University of Tennessee, Knoxville, Tennessee 37996-1200
and Oak Ridge National Laboratory, Oak Ridge, Tennessee 37831

N. Stolterfoht, H. Schmidt-Böcking, G. Nolte, and G. Schiwietz
Hahn-Meitner-Institut für Kernforschung, D 1000 Berlin 39, Federal Republic of Germany
(Received 23 July 1984)

A general purpose projectile-frame expansion fitting method is used to characterize the shape of the electron capture to the continuum (ECC) cusp for bare carbon, oxygen, neon, and argon projectiles, incident on atomic and molecular hydrogen, and helium targets, over the velocity range 6—18 a.u. The method used to fit the ECC cusp shape allows the direct comparison of spectra taken under differing instrumental conditions in an apparatus-independent manner. The results reveal a substantial similarity in the ECC cusp shape for a wide variety of projectile Z, projectile velocity, and target combinations which has not yet been explained by current theories which predict the shape of the ECC cusp.

INTRODUCTION

The velocity spectrum of electrons ejected into the forward direction in energetic ion-atom collisions exhibits a cusp-shaped peak when the emergent electron velocity $\mathbf{v}_e$ matches that of the outgoing ion velocity $\mathbf{v}_p$ in both speed and direction. For bare or nearly bare incident projectile ions, the electrons arise from transfer of a target electron to a low-lying projectile-centered continuum state (ECC), whereas if there are loosely bound projectile electrons available, those electrons can be lost to similar low-lying continuum states; the process is then termed electron loss to the continuum (ELC). Since the discovery[1] of these processes, known collectively as electron transfer to the continuum (ETC), there has been increased interest in both the experimental and theoretical aspects of this problem, and there exist several reviews of research in ETC.[2,3]

In early theories[4,5] a first-order perturbative treatment of the charge exchange amplitude was used to explain the ECC cusp. Within this approximation the final electronic state was considered to be described in terms of a simple Coulomb wave centered on the projectile, leading to a cusp nearly symmetric in $\mathbf{v}_e - \mathbf{v}_p$. However, later experimental results for both bare heavy projectiles[6] and hydrogen projectiles[7] showed a skewness of the ECC peak shape toward lower electron velocities.

To account for this asymmetry, the distortion of the outgoing electronic state by the interaction between the cusp electron and the residual ion must be considered, but in a way which goes far beyond a simple post-collision interaction description. In 1978 Shakeshaft and Spruch (SS) included a second-order term in the Born expansion[8] to approximate this effect in their calculation of the ECC cusp shape in a hydrogenic-target approximation, while Chan and Eichler (CE) proposed that a more careful calculation within the first-Born-approximation framework could account for the cusp skewness.[9] Subsequent experiments[10,11] confirmed a cusp asymmetry whose properties were more similar to that predicted by SS as opposed to the CE results, but the strong dependence of the asymmetry upon projectile Z and velocity in the SS theory was not found. In addition, the SS approach predicts a negligible asymmetry for singly ionized projectiles, which to the extent that a hydrogenic-target approximation may be valid (to our knowledge all previously published results have used targets with two or more electrons) has been contradicted by experiments.[7,12]

In later theoretical works, Miraglia and Ponce[13,14] discuss the details of the leading anisotropic contributions to the cusp shape within the second Born approximation, again in a hydrogenic-target approximation, but their use of free-particle Green's functions as opposed to Coulomb Green's functions to characterize the interaction probably limits the application to projectiles lighter than those considered in this paper. Garibotti and Miraglia[15] present results originating from the first-order term of a multiple scattering theory, which lead to a cusp shape similar to that of SS. This treatment also uses free-particle Green's functions, so its application is likely limited in the same way. Because all of their theories treat hydrogenic targets, the comparison for molecular hydrogen and helium targets may require modification.

Very recently, Jakubassa-Amundsen calculated the shape of the ECC cusp within the semiclassical impact approximation[16] (SCIA) for the case of argon projectiles and helium targets, and the resulting shape compares well with experiment.[11] This approach goes beyond the second Born approximation, incorporating the effects of large perturbing fields present in collisions involving highly charged projectiles, as well as making allowance for a weaker, target-atom—continuum-electron interaction. The promising results of this work indicate that extending

the results to other incident ion species and impact energies would be desirable.

In this paper we present a more detailed discussion of helium-target results briefly presented previously,[10] as well as newer results more recently completed, in which both atomic and molecular hydrogen targets are also included. By using a general, model-independent method[12,17] for theoretically describing the cusp shape that explicitly takes into account the effect of a given experimental choice of analyzer geometry, resolution, and angular acceptance, we can compare spectra from different experiments directly and extract the basic underlying shape of the ECC cusp as parametrized by the general theory.[12,10] In addition, previously published data for helium targets[6,11] are analyzed by this procedure to give a more complete description of the variation of the ECC cusp shape on the impact velocity and with the ion and target species.

EXPERIMENTAL PROCEDURE

The bare projectile ion beams necessary for this experiment were obtained from accelerators at Brookhaven National Laboratory (BNL), Lawrence Berkeley Laboratory (LBL), Hahn-Meitner-Institut (HMI), and Oak Ridge National Laboratory (ORNL). The schematic diagram presented in Fig. 1 shows a typical experimental arrangement, and Table I lists some of the important parameters applicable to the different experiments.

The projectile beams, typically delivering a few particle nanoamperes of current on target, were passed through two sets of collimating slits or apertures which determined the beam diameter at the entrance focus of the analyzer and limited the beam angular divergence to $\lesssim 0.1°$. In those cases in which the beam energy exceeded the Coulomb barrier for spectrometer materials a carbon skimmer aperture slightly larger than the beam diameter (typically 1.5 mm) was placed between the last collimator and the target gas cell to prevent scattered ions and electrons generated at slit edges from striking the spectrometer. In addition, this aperture was followed by a transverse electrostatic field of ~ 3 kV/cm, which was found necessary to remove additional electrons traveling collinearly with the projectile ions.

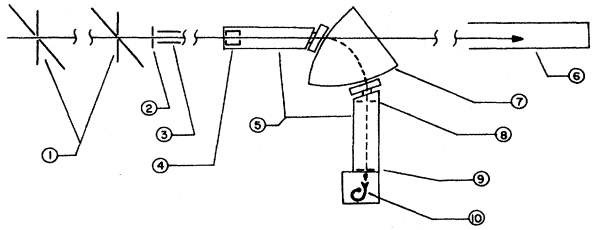

FIG. 1. Schematic diagram of experimental arrangement with magnetic sector spectrometer. Solid line indicates the path of the projectile ion beam, and the broken line shows a typical electron path through the analyzer. (1) Four-jaw carbon slits to define beam spot size and angular divergence. (2) Carbon skimmer aperture to eliminate beam halo. (3) Electric field plates to remove electrons produced at slits. (4) Target cell. (5) Magnetic shielding for electron drift region. (6) Faraday cup. (7) Spectrometer field plates. (8) Angle limiting aperture. (9) Image aperture to determine velocity resolution. (10) Channel-electron-multiplier detector.

The ion beam then traversed a cylindrical gas cell containing the target gas species, the center of which was located at the entrance focus of either a 90° second-order double-focusing magnetic sector spectrometer or a 160° spherical sector analyzer. In the former case the central-ray bending radius was 61.3 mm, while in the latter it was 54.7 mm. The gas-cell pressure was established by a feedback-controlled capacitance manometer system and was maintained at pressures within single-collision conditions. For the data concerning atomic and molecular hydrogen targets, the target cell consisted of a hydrogen dissociation oven.

The novel design features of the electron-impact heated dissociation oven are currently in preparation for publica-

TABLE I. Instrumental and other experimental parameters. Refer to Fig. 5 for an explanation of FWHM, TW, and θ_0.

Location	Projectile	Energy (MeV)	Velocity (a.u.)	Target	Analyzer	FWHM (%)	TW (%)	θ_0 (deg)
ORNL EN Tandem	C^{6+}	12	6.3	H H_2	Elec.	1.1	1.1	2.0
BNL MP Tandem	O^{8+}	30 40	8.7 10.0	He	Elec.	1.3	0.0	1.8
ORNL HHIRF Tandem	O^{8+}	94 110 125	15.4 16.6 17.2	He	Mag.	0.7	0.0	1.4
HMI VICKSI Cyclotron	Ne^{10+}	155	17.6	He	Mag.	1.1	0.0	1.4
LBL Super Hilac	Ar^{18+}	236 340	15.0 18.1	He	Mag.	1.7	0.0	1.5

tion elsewhere,[18] so only a brief description follows. Figure 2 shows a simplified schematic drawing of the hydrogen dissociation apparatus. A focused electron beam (typically 200 mA at 6 kV) extracted from a tungsten dispenser cathode is directed through a mounting tube to strike a hollow tungsten plug containing hydrogen gas. The tungsten plug reaches a temperature in excess of 2400 K, producing a dissociation fraction (fraction of molecules dissociated) of approximately 50% (twice as many atomic targets as molecular targets) to 90% over the range of target gas densities used in our experiments. The low electron current produces a magnetic field of $\lesssim 40$ mG, at the position of the target, which is further reduced inside the spectrometer by magnetic shielding enclosing the spectrometer. At the analyzer resolution level used for our experiments, fields $\lesssim 40$ mG do not perceptibly affect the cusp shape or yield. The entire oven assembly is mounted within a water-cooled copper jacket which shields the analyzer and channel-electron-multiplier detector from both heat and stray high-energy electrons.

After traversing the target cell, the projectile beam and accompanying electrons enter the analyzer along the central ray; the ions exit the analyzer through an exit hole (diameter typically 3 mm) and pass into a Faraday cup (located several meters away when nuclear reactions between the beam ions and the Faraday cup material were of concern). The electrons traveling at the velocity set by the analyzer field were focused on an aperture placed at the spectrometer exit focus (typical diameter 1.5 mm) which together with the beam diameter at the target gas-cell center as defined by the beam collimation ("virtual" entrance aperture) determined the energy or momentum resolution of the analyzer. A second aperture placed in the field-free region of the electron path downstream of the analyzer field limited the collection cone of the spectrometer, and those electrons passing through the apertures were detected by a channel electron multiplier (CEM). The entire analyzer region was placed at the center of three orthogonal coil pairs, which reduced the external magnetic fields over the electron path to $\lesssim 30$ mG.

The electron counts were collected and stored in a standard multichannel scaling (MCS) arrangement, in which a fixed ion charge was used to step the spectrometer field over the desired electron velocity range. When the energy of the projectile beam was in excess of the Coulomb barrier, a nuclear radiation background ($\sim 25\%$) was present, due primarily to γ rays originating from the collimation slits which in turn produced photoelectrons in the vicinity of the target gas cell and at other illuminated surfaces such as the interior surfaces of the analyzers. To correct for this effect, so-called "gas dump" spectra were acquired, when the same gas flux necessary to maintain target cell pressure was routed directly into the experimental chamber, producing the same chamber pressure and leaving all other conditions fixed. Similar backgrounds due to photons emitted by the hydrogen dissociation oven internally striking the larger radius plate of the analyzer and producing detectable spurious photoelectrons were removed in the same way. In the other experimental cases no significant backgrounds were present. In Fig. 3 a typi-

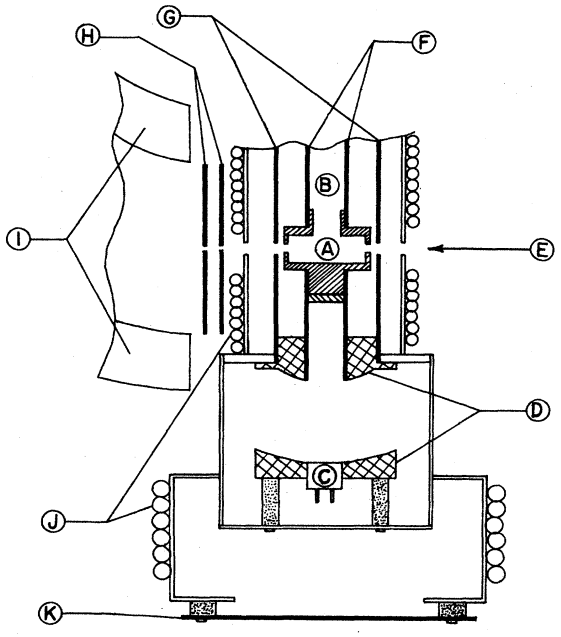

FIG. 2. Simplified diagram of atomic hydrogen dissociation oven apparatus (drawing not to scale). (*A*) Tungsten oven assembly including replaceable "wear" plug at point where high-energy electrons strike. (*B*) Gas inlet. (*C*) High-current dispenser cathode. (*D*) Spherical acceleration lens. (*E*) Ion beam path. (*F*) Tungsten inner radiation shield-support tube. (*G*) Outer radiation shields. (*H*) Photon limiting apertures. (*I*) Spherical sector electron spectrometer deflection plates. (*J*) Water-cooled copper-jacket—support assembly. (*K*) Bias plate to allow pumping of cathode region without allowing stray electrons to escape.

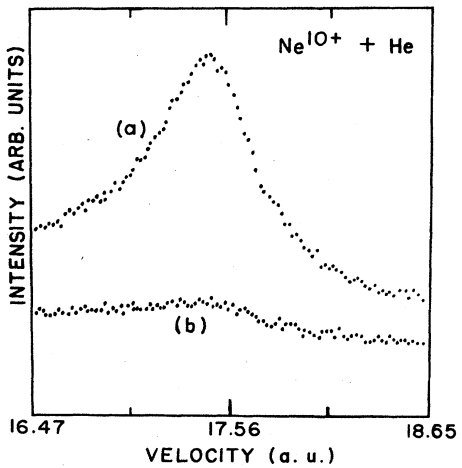

FIG. 3. (a) Longitudinal ECC velocity spectrum including nuclear radiation background for 155-MeV bare neon projectiles incident on helium gas in the target cell. (b) Equivalent electron velocity spectrum taken with the same mass flow of helium introduced directly into the spectrometer chamber ("gas dump" mode). Difference spectrum resulting from subtracting (b) from (a) was used in the cusp fitting procedure described later.

cal spectrum and its associated background (here primarily nuclear) is shown.

CUSP-SHAPE ANALYSIS

The generally accepted form of the cross section for ETC electrons ejected in the forward direction with velocities close to that of the incident ion[17] is given by

$$\frac{d\sigma}{d\mathbf{v}} \propto \frac{f(v_e,v_p,\theta_e)}{|\mathbf{v}_e-\mathbf{v}_p|} , \tag{1}$$

where $f(v_e,v_p,\theta_e)$ is finite for $\mathbf{v}_e=\mathbf{v}_p$ and with $v_e=|\mathbf{v}_e|$, $v_p=|\mathbf{v}_p|$ and θ_e, as indicated in Fig. 4. The projectile ion velocity $\mathbf{v}_p$ is assumed to lie along the positive Z axis (its trajectory essentially unchanged by the collision), and the primed variables refer to the electron in the projectile frame.

The denominator of Eq. (1), symmetric about $\mathbf{v}_e=\mathbf{v}_p$, gives rise to the "cusp" shape and results from the Coulomb interaction between the outgoing projectile ion and the ejected electron. The function $f(v_e,v_p,\theta_e)$ can incorporate the observed asymmetry, and as in Refs. 12 and 17 we expand it in terms of a projectile-frame "partial-wave" expansion,

$$f(v_e,v_p,\theta_e)=\tfrac{1}{2}\pi^{-1/2}\sum_l (2l+1)^{1/2}a_l P_l(\cos\theta_e') . \tag{2}$$

Note that this is a partial-wave expansion of the *cross section,* and not that of a wave-function amplitude, as is more commonly the case. The coefficients a_l are now functions only of v_e and v_p (for given ion and target Z), and since $v_e'=|\mathbf{v}_e-\mathbf{v}_p|$ is small in the neighborhood of the cusp peak, the a_l may be expanded in a Taylor series in v_e', resulting in

$$\frac{d\sigma}{d\mathbf{v}}=\frac{C}{v_e'}\sum_{n,l} B_{n,l}(v_p)(v_e')^n P_l(\cos\theta_e') , \tag{3}$$

where $B_{0,0}\equiv 1$.

To compare the cross section with the measured distributions $Q(v_e,\theta_e)$, the product of the spectrometer acceptance function $S(v_e,\Omega_e)$ and the cross section $d^2\sigma/dv_e d\Omega_e=(v_e)^2(d\sigma/d\mathbf{v})$ are integrated over the experimental acceptances in velocity and angle, resulting in

$$Q(v_e,\theta_e)=C\sum_{n,l} B_{n,l}(v_p) \times\int_{v_e}\int_{\Omega_e}(v_e)^2(v_e')^{n-1}P_l(\cos\theta_e') \times S(v_e,\Omega_e)dv_e d\Omega_e . \tag{4}$$

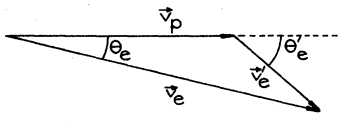

FIG. 4. Vector diagram indicating the relationship between the projectile frame variables (primed) and the laboratory frame variables (unprimed). Subscript p refers to the projectile ion and subscript e to the unbound ECC electron.

This is the appropriate functional form for use with the magnetic analyzer, for the electrostatic analyzer $S(v_e,\Omega_e)$ is replaced by $S(E_e,\Omega_e)$ and $d^2\sigma/dv_e d\Omega_e$ by $d^2\sigma/dE_e d\Omega_e=(v_e/\mu_e)(d\sigma/d\mathbf{v}_e)$ to get the resulting $Q(E_e,\theta_e)$ (μ_e is the reduced mass of the ejected-electron—target-nucleus system).

The variations in experimental conditions summarized in Table I are incorporated in the transmission functions S. We assume that for small velocity resolutions ($R\equiv\delta v/v\lesssim 2\%$) and for maximum polar acceptance angles ($\theta_0\lesssim 2°$) the transmission functions are separable:

$$S(v_e,\Omega_e)=R(v_e)G(\theta_e) . \tag{5}$$

Meckbach *et al.*[12] have verified that Eq. (5) is an excellent approximation. From measurements with monoenergetic electron beams, we have also determined that $R(v_e)$ is well approximated by a triangular or trapezoidal line shape [Fig. 5(a)]. In Fig. 5(b) we show a typical $G(\theta_e)$ numerically calculated from the geometrical arrangement of limiting apertures and the rectangular functional approximation used for fitting calculations. By using this approximation the integrals over angle become elementary, and calculation speed is greatly enhanced with little effect on the folded cusp line shape.

To determine the best-fit values of $B_{n,l}$ for the cross-section expansion given in Eq. (3), the value of Eq. (4) was calculated for trial values of the coefficients ($B_{n,l}$) and the angle θ_0, as shown in Fig. 5(b), and the resulting function was fitted to the experimental data distributions using a least-squares-fitting procedure. Only those coefficients with $n=0,1$ and $l=0,1,2$ were needed for the fits to

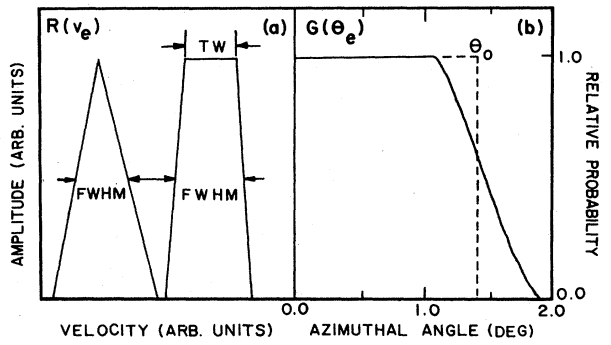

FIG. 5. (a) Examples of triangular (left) and trapezoidal (right) electron velocity resolution functions $R(v_e)$ used to characterize the transmission of the electron spectrometer for a fixed internal deflecting field. The top width (TW) and full width at half maximum (FWHM) which describe $R(v_e)$ are listed in Table I for each of the different measurements included in this paper. (b) $G(\theta_e)$, the relative angular transmission function (as compared to a case with no angle limiting aperture) for the laboratory-frame azimuthal angle θ_e. The solid curve is calculated from purely geometrical considerations for an angle limiting aperture of 5.5 mm and an image (exit) aperture of 1.5 mm separated by 106 mm. The dashed curve shows the rectangular approximation used with the resulting value of θ_0 as determined by the fitting procedure for the case of 94-MeV oxygen projectiles.

converge to their approximate best-fit conditions. As discussed in Ref. 12, this limits the validity of Eq. (3) to intermediate and high ion energies. In Fig. 6 the terms of Eq. (4) for a given coefficient are displayed for comparison with all amplitudes $B_{n,l}$ set to 1 and a δ-function line shape $R(v_e)$; the terms corresponding to $l=0$, 1, and 2 are labeled (solely for convenience) S_n, P_n, and D_n, respectively.

The full width at half maximum (FWHM) and top width (TW) which described the velocity (or energy) linewidth $R(v_e)$ were fixed during the fitting procedure at the values determined by electron-gun calibration data. The cutoff value θ_0 of the angular acceptance function $G(\theta_e)$ was allowed to vary, but in all cases the final value was in good agreement (to within five percent) with that directly calculated from geometrical considerations.

In Table II a summary of the numerical results of the fitting procedure for the various combinations of projectile and target species is presented. Within parentheses beside values for each $B_{n,l}$ one-standard-deviation variances are listed for those cases in which the amount of data permitted fits to multiple data sets; in all other cases best-fit results were found by summing all data into a single spectrum for fitting.

In two cases presented in Table II the reduced χ^2 value indicating the "goodness of fit" exceeds 4.0, whereas all other fits have χ^2 values near 1.0. The 10.0-a.u. helium-target data have a large value which is not unreasonable in view of the limited counting time and small cross section for this particular spectrum; the cusp was recorded originally only for determining the yield integrated over a ±4% velocity range. The atomic-hydrogen-target data were taken under somewhat adverse conditions: The total data rate was about two counts per second, of which about 60% of the counts recorded represented photoelectron backgrounds. Of the remaining counts, part of the signal was due to the remaining fraction of molecular hydrogen targets, leaving only a very small signal attributable to atomic hydrogen cusp electrons. It would indeed be difficult to improve these results, as the blackbody radiation from the incandescent oven creates an intense flux of photoelectrons comparable to the flux of cusp electrons.

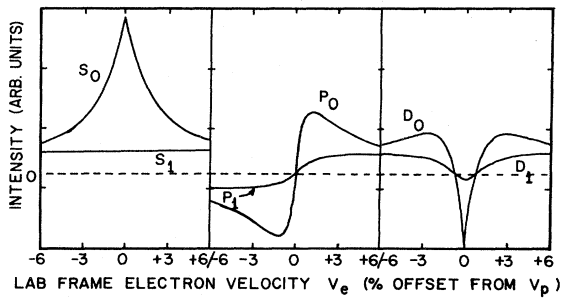

FIG. 6. Examples of the cusp-shape contributions from the six lowest-order terms of the cross-section expansion used to characterize the laboratory-frame ECC cusp shape. These are displayed for normalized amplitudes $B_{n,l}=+1$. Values of $\theta_0=1.4°$ and a δ-function $R(v_e)$ velocity linewidth were assumed for the analyzer parameters here. The velocity scale is represented in terms of the percentage difference between the laboratory-frame electron and projectile velocities.

As a check for systematic errors in the fitting procedure, variance spectra from the fits were recorded. Each channel of the variance spectrum contained that channel's contribution to the χ^2 for the fit, multiplied by the sign of the difference between the data and fit values. This approach to characterizing the deviation of the fit was preferred to using a simple difference spectrum, since the large variation of the cusp amplitude between the peak and the wings causes the latter approach to overstate the fit error. This overstatement is traceable to the fact that the much higher counting statistics in the neighborhood of the cusp peak imply that the shape of the cusp is better determined experimentally in the vicinity of the cusp

TABLE II. Results of fits for several targets and projectiles. The coefficients are explained in the text; the coefficient for the dominant S_0-component is normalized to 1. Errors (in parentheses) where given are 1 standard deviation derived from multiple fits.

Projectile	Target	Velocity (a.u.)	Fit angle (deg)	S_1	P_0	P_1	D_0	D_1	χ^2
C	H	6.3	2.14	0.32	−0.42	−0.37	−0.03	−0.21	4.94
	H_2		1.97	−0.20	−0.48	−0.08	−0.07	0.01	1.09
O	He	8.6	1.83	0.23	−0.25	−0.40	−0.25	0.07	1.23
		10.0	1.73	−0.17	−0.37	−0.05	−0.06	−0.05	4.29
		15.4	1.41	0.22	−0.49	−0.04	−0.03	0.00	1.63
				(0.11)	(0.03)	(0.01)	(0.03)	(0.02)	(0.24)
		16.6	1.40	0.08	−0.47	−0.05	0.10	0.12	1.23
				(0.19)	(0.04)	(0.08)	(0.10)	(0.10)	(0.34)
		17.2	1.40	0.02	−0.48	−0.02	0.03	0.02	1.30
Ne	He	17.6	1.65	0.01	−0.47	−0.02	0.02		1.49
				(0.01)	(0.03)	(0.01)	(0.01)		(0.22)
Ar	He	15.0	1.45	0.57	−0.39	−0.26	−0.17		1.0
		18.1	1.41	0.43	−0.47	−0.12	−0.17		1.4

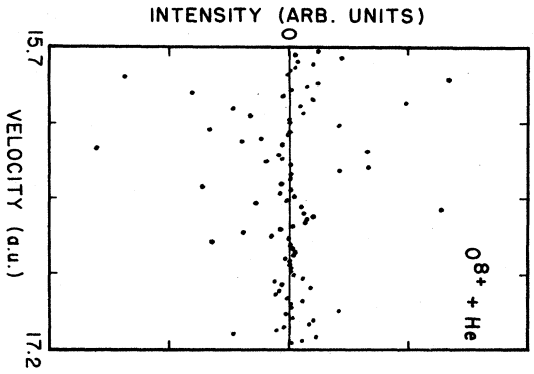

FIG. 7. Variance spectrum (see text for explanation) for 94-MeV bare oxygen projectiles and helium-target gas.

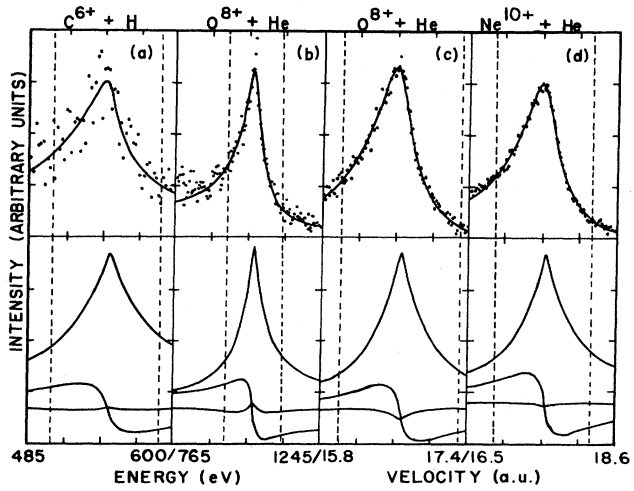

FIG. 8. The top row shows four comparisons between fitted spectra (solid lines) and data (dots) incorporating background subtraction where appropriate for (a) 12-MeV bare carbon projectiles, (b) 30-MeV and (c) 110-MeV bare oxygen projectiles, and (d) 155-MeV bare neon projectiles. The vertical dashed lines indicate equivalent arbitrary $(1\pm0.04)v_p$ limits for each of four spectra. The bottom row displays S, P, and D components of the fitted function (summed over both $n=0,1$, components) for the corresponding fitted function shown above. The bottom spectra have been displayed with a δ-function linewidth to remove the dependence of the cusp shape on the particular experimental linewidth, allowing for a more direct comparison of the results.

peak. In Fig. 7 an example of the variance spectra is displayed. The symmetrical scatter of the spectrum values about zero are indicative of the lack of systematic errors in the method chosen to quantify the cusp shape. A similar lack of systematic error in the fit was found for all of the data presented here.

RESULTS AND CONCLUSIONS

The most striking feature of the results presented in Table II is the remarkable consistency of the values found for the major asymmetric term P_0, for the wide variety of target and projectile combinations used in these experiments ($8 \leq Z_p \leq 18$; $Z_t = 1,2$; $6 \leq v_p \leq 18$). As discussed by Macek *et al.*,[17] the presence of this term implies the necessity of second-Born-approximation terms in any theoretical description, as in the approach of Shakeshaft and Spruch.[8] However, the strong dependence of the asymmetry on Z_p, Z_t, and v_p in their theory (in a hydrogenic target-electron approximation) is not evident. The cases in which this term is not as significant occur for helium targets and incident ion energies for which the ratio of the incoming ion velocity to the target-electron velocity (K-shell velocity) is the smallest (about 4 and 5, respectively), suggesting that asymptotic velocities have not yet been reached.

The S_1 term shows a large percentage variation in values found from the fitting procedure, but the effect on the overall shape is minor because of the size of this term compared to the dominant S_0 term, especially at the cusp peak. This variation is most likely caused by errors in background subtraction, the accuracy of which was sensitive to slight variations in beam steering conditions. The D-term values found in all cases are also small and are mainly important to the fit in the wings of the cusp where $v_e' \ll 1$ is not as valid.

In Fig. 8 we present representative fit results for helium targets, as well as those for atomic hydrogen (the contribution of molecular targets has been subtracted), and the resulting S, P, and D component parts of each fit. The similarity of the cusp shape for both helium and hydrogen targets suggests that at least for the velocities considered here the results for helium targets approximate those for atomic hydrogen targets at a satisfactory level.

We hope that presenting our results in a model-independent manner, which attempts to account for the variations in experimental arrangements, will serve as a stimulus for further theoretical investigation into the shape of the ECC cusp, especially the detailed dependence of the asymmetry on Z_p, Z_c, and v_p in view of the results given here. In particular, the promising approach of Jakubassa-Amundsen[16] in explicating the argon projectile data in Ref. 11 warrants application of her method to the combinations of projectile Z and v discussed in this paper. Also, it is our expectation that by making further systematic studies of the cusp shape, especially as a function of collection angle, and describing the results in an equivalent manner, more insight into the nature of the ECC cusp asymmetry and its theoretical explanation will be possible.

As a final note, questions have been raised concerning the relative importance of analyzer field-ionized Rydberg states in determining the shape of the cusp in an ETC process. Vager *et al.*[19] suggested this process was responsible for a significant fraction of the cusp yield, based on an experiment performed using light projectiles passing through foil targets. However, several authors[20] disagreed with this conclusion. More recent work by our group[21] indicates that for the experimental arrangements we have always used, the fraction of electrons originating from field-ionized Rydberg states is insignificant for angular acceptances of $\geq 1°$. Only by placing the target a considerable distance of about 20 cm from the entrance focus of

our analyzer, and thereby drastically reducing the effective angular acceptance of our spectrometer to a very small value ($\sim 0.1°$), approximating the arrangement of Vager *et al.*, did the Rydberg-electron yield become appreciable. Since the ETC cusp yield depends strongly on the angular acceptance and the Rydberg yield is approximately constant, the fraction of Rydberg electrons detected becomes quite small ($\lesssim 2\%$) for the acceptance angles used here (1°—2°). Furthermore, for a given analyzer field the use of larger projectile Z here reduces the field ionization of Rydberg states of the projectile ions, making the Rydberg fraction even smaller.

ACKNOWLEDGMENTS

We would like to thank the coauthors of Refs. 6, 10, and 11 for their contributions to previously published data, some of which are incorporated here. Also, we wish to thank the staffs at each of the accelerators at BNL, LBL, HMI, and ORNL for their able assistance in performing this series of experiments, and J. Burgdörfer for many valuable discussions pertaining to the theoretical aspects of this work. This research was supported by the National Science Foundation; the U.S. Department of Energy, under Contract No. DE-AC05-84OR21400 with Martin Marietta Energy Systems, Inc.; and Deutche Forschungemeinschaft and Bundes Ministerium für Forschung und Technologie in West Germany. The results pertaining to hydrogen targets were supported by the Fundamental Interactions Branch, Division of Chemical Sciences, Office of Basic Energy Sciences, of the U.S. Department of Energy, under Contract No. DE-AS05-79ER10512.

---

*Current address: Naval Surface Weapons Center, White Oak, Silver Spring, Maryland 20910.

†Permanent address: Institut für Kernphysik, Universität Frankfurt, August-Euler-Strasse, D 6 Frankfurt am Main, Federal Republic of Germany.

‡Permanent address: Physics Institute, University of Aarhus, DK-8000 Aarhus C, Denmark.

§Current address: University of Colorado, Boulder, Colorado 80302.

[1]G. B. Crooks and M. E. Rudd, Phys. Rev. Lett. **25**, 1599 (1970); K. G. Harrison and M. Lucas, Phys. Lett. **33A**, 149 (1970).

[2]W. Meckbach and R. A. Baragiola, in *Inelastic Ion-Surface Collisions,* edited by N. M. Tolk, J. C. Tully, W. Heiland, and C. W. White (Academic, New York, 1977), p. 283; I. A. Sellin, J. Phys. (Paris) **40**, Cl-255 (1979); C. R. Vane, IEEE Trans. Nucl. Sci. **NS-26**, 1078 (1979); M. W. Lucas, in Proceedings of the Workshop on Physics with Fast Molecular-Ion Beams, edited by D. S. Gemmell (Argonne National Laboratory Report No. ANL/PHY-79-3, 1979), p. 291; V. H. Ponce and W. Meckbach, Comments At. Mol. Phys. **10**, 231 (1981); I. A. Sellin, in *Proceedings of the Twelfth International Conference on the Physics of Electron and Atomic Physics, Gatlinburg, 1981,* edited by S. Datz (North-Holland, Amsterdam, 1982); K.-O. Groeneveld, W. Meckbach, I. A. Sellin, and J. Burgdörfer, Comments At. Mol. Phys. **14**, 187 (1984).

[3]M. Breinig, S. B. Elston, S. Huldt, L. Liljeby, C. R. Vane, S. D. Berry, G. A. Glass, M. Schauer, I. A. Sellin, G. D. Alton, S. Datz, S. Overbury, R. Laubert, and M. Suter, Phys. Rev. A **25**, 3015 (1982).

[4]J. Macek, Phys. Rev. A **1**, 235 (1970); W. J. B. Oldham, Phys. Rev. **161**, 1 (1967); A. Salin, J. Phys. B **5**, 979 (1972).

[5]K. Dettmann, K. G. Harrison, and M. W. Lucas, J. Phys. B **7**, 269 (1974).

[6]C. R. Vane, I. A. Sellin, M. Suter, G. D. Alton, S. B. Elston, P. M. Griffin, and R. S. Thoe, Phys. Rev. Lett. **40**, 1020 (1978).

[7]M. Rødbro and F. D. Andersen, J. Phys. B **12**, 2883 (1979).

[8]R. Shakeshaft and L. Spruch, Phys. Rev. Lett. **41**, 1037 (1978).

[9]F. T. Chan and J. Eichler, Phys. Rev. A **20**, 367 (1979); R. Shakeshaft and L. Spruch, *ibid.* **20**, 376 (1979).

[10]S. D. Berry, I. A. Sellin, K.-O. Groeneveld, D. Hofmann, L. H. Andersen, M. Breinig, S. B. Elston, M. M. Schauer, N. Stolterfoht, H. Schmidt-Böcking, G. Nolte, and G. Schiwietz, IEEE Trans. Nucl. Sci. **NS-30**, 902 (1983).

[11]M. Breinig, S. Elston, I. A. Sellin, L. Liljeby, R. Thoe, C. R. Vane, H. Gould, R. Marrus, and R. Laubert, Phys. Rev. Lett. **45**, 1689 (1980).

[12]W. Meckbach, I. B. Nemirovsky, and C. R. Garibotti, Phys. Rev. A **24**, 1793 (1981).

[13]J. E. Miraglia and V. H. Ponce, J. Phys. B **13**, 1195 (1980).

[14]V. H. Ponce, J. Phys. B **14**, 3463 (1981).

[15]C. R. Garibotti and J. E. Miraglia, J. Phys. B **14**, 863 (1981).

[16]D. H. Jakubassa-Amundsen, J. Phys. B **16**, 1767 (1983).

[17]M. W. Lucas, W. Steckelmacher, J. Macek, and J. E. Potter, J. Phys. B **13**, 4833 (1980); J. Macek, J. E. Potter, M. M. Duncan, M. G. Menendez, M. W. Lucas, and W. Steckelmacher, Phys. Rev. Lett. **46**, 1571 (1981).

[18]G. A. Glass, Ph.D. thesis, University of Tennessee, 1984; G. A. Glass (unpublished).

[19]Z. Vager, B. J. Zabransky, D. Schneider, E. P. Kanter, Gu Yuang Zhuang, and D. S. Gemmell, Phys. Rev. Lett. **48**, 592 (1982).

[20]M. W. Lucas, W. Steckelmacher, and J. Macek, Phys. Rev. Lett. **50**, 1014 (1983); I. B. E. Nemirovsky, W. Meckbach, and P. Foche, *ibid.* **50**, 1015 (1983); M. Breinig, S. B. Elston, S. D. Berry, G. A. Glass, I. A. Sellin, and C. R. Vane, *ibid.* **50**, 1016 (1983).

[21]P. Engar, M. Breinig, R. DeSerio, I. A. Sellin, C. E. Gonzalez-Lepera, S. D. Berry, M. Bloemer, and T. Underwood, *Satellite Workshop and Conference Abstracts,* Ninth International Conference on Atomic Physics, Seattle, 1984, edited by Robert S. Van Dyck, Jr. and E. Norval Fortson (University of Washington, Seattle, in press), p. A41.